# Impingement of a circular liquid jet on a moving wall

Xiaohe Liu,[1] Neil J. Balmforth,[2] Boris Stoeber,[1,3] and Sheldon Green[1]
[1)]*Department of Mechanical Engineering, University of British Columbia.*
[2)]*Department of Mathematics, University of British Columbia.*
[3)]*Department of Electrical and Computer Engineering, University of British Columbia.*

(*Electronic mail: sheldon.green@ubc.ca.)

(Dated: 5 December 2022)

The impingement of a liquid jet onto a moving wall can lead to deposition in which fluid spreads into a steady, U-shaped lamella. Experiments are conducted using a rotating disk that can produce jet Reynolds numbers $15 \leq Re_j \leq 16{,}000$ and wall-to-jet velocity ratios $0.04 \leq u_w/v_j \leq 14$, under conditions under where the effects of surface tension and gravity are relatively minor. High speed video and Laser-Induced-Fluorescence are used to measure the geometry of the impinging jet. The experiments are complemented with numerical simulations, which reveal the anatomy of the lamella: the jet is diverted sideways by pressure gradients over an impact zone that has a radius of order the jet diameter. Viscous stresses play little role in the diversion of incoming fluid, but act outside the impact region to turn the flow towards the direction of motion of the wall. A fraction of the viscously redirected fluid is thereby taken back underneath the jet, cushioning its impact. Eventually, the fluid enters a downstream region of almost uniform depth wherein all the fluid is conveyed with the wall. A simple model is proposed to rationalize the U-shape of the lamella, fixing that footprint by arguing that this arises where the radially symmetric, viscously modified outflow from the jet matches the wall velocity. The simple model predicts the dimensions of the lamella (the length of the upstream heel and the width of the downstream lamella), and that the shape takes a universal form when scaled by one of these distances. These predictions agree well with the experiments and simulations, except when the heel becomes excessively small.

## I. INTRODUCTION

The impingement of a circular liquid jet on a stationary surface has been studied extensively: Schach[1] presented a theoretical analysis of the potential flow problem for inviscid jet impingement, with later developments presented by Refs. 2–4. Subsequent work[5–9] considered the impact of viscosity, gravity and surface tension within the framework of boundary-layer theory, predicting the position where a hydraulic jump forms due to a downstream obstruction.

The axisymmetry of circular liquid jet impingement can be broken in several ways. For example, Kate et al.[10] studied the impact of a jet impinging at an angle to the substrate, and Wilson and co-workers have explored the action of gravity on the impingement of a horizontal jet onto a vertical wall[11–13]. Here, we consider how the circular symmetry is broken when a liquid jet impinges onto a moving wall, continuing on from a previous study exploring the corresponding planar (*i.e.* two-dimensional) problem.[14,15] Such problems are of interest to a variety of industrial applications, ranging from surface coating, cooling and cleaning[16–20] to the deposition of liquid friction modifiers in the railroad industry[21,22].

At very low Reynolds numbers, viscous stresses bend the jet before it makes contact with the wall, and instabilities analogous to elastic buckling lead to a variety of patterns that have been referred to as a "fluid mechanical sewing-machine"[23,24]. At much higher Reynolds numbers, the jet remains largely unaffected by viscosity, with impact pressures diverting the incoming fluid into a spreading sheet. In this situation, one expects two possible outcomes: splash, or the deposition of a thin film (a lamella) onto the moving surface. Moreover, once viscosity exerts its effect on any lamella, the recirculation of fluid back towards the jet forms a downstream obstruction (relative to the jet motion away from the impingement location) that sets the scene for the appearance of hydraulic jumps. Previous experiments have, indeed, observed these different possible outcomes[25–30].

Much of the previous work has focused on transition from deposition to splashing, categorizing the impact of the speed and properties of the incoming liquid jet, the speed and roughness of the wall, and the ambient air pressure[25–28]. Our focus here is rather on the deposition regime under conditions where surface tension and gravity are less significant, for which previous experiments have indicated that the fluid spreads into a distinctive U-shaped lamella reminiscent of the Rankine half-body in potential flow[29,30]. In this setting, and given the jet diameter and speed, $d$ and $v_j$, the wall speed, $u_w$, and the fluid density and viscosity, $\rho$ and $\mu$, the two key dimensionless parameters that control the problem are the jet Reynolds number $Re_j = \rho v_j d/\mu$, and the velocity ratio $u_w/v_j$.

We use a combination of laboratory experiments and numerical simulations to explore the regime of steady deposition. Our first goal is to establish a regime diagram on the $(Re_j, u_w/v_j)$ plane that identifies where jet impingement onto a moving surface creates a steady U-shaped lamella. We further focus on situations in which viscous stresses are sufficiently strong and wall speeds are sufficiently high that turbulence and hydraulic jumps are mostly avoided. The U-shaped lamella then adopts a relatively simple structure that we characterize in detail. In particular, we observe that the lamella downstream of the jet is relatively flat and the U-shape has a scale that varies with $Re_j$ and $u_w/v_j$ but otherwise takes a nearly universal form (somewhat like the Rankine half-body).

In Section II A, we describe the experimental approach. The numerical method is summarized in Section II B. We report the observed phenomenology of the jet impact and the regime diagram in Section III. A simple model that captures the U-shape of the lamella is formulated in Section IV. We

compare the model predictions and the results from the experiments and simulations in Section V. We close with brief conclusions, open questions and suggestions for future work in Section VI.

## II. METHODOLOGY

### A. Experimental Approach

#### 1. *Apparatus*

As sketched in Fig. 1, the experiment consists of a disk spun on a horizontal axis, an accumulator attached to a nozzle assembly, high-speed cameras, and laser optics. The different experimental components are controlled via LabVIEW. All experiments are conducted at an atmospheric air pressure of $101 \pm 1.5$ kPa.

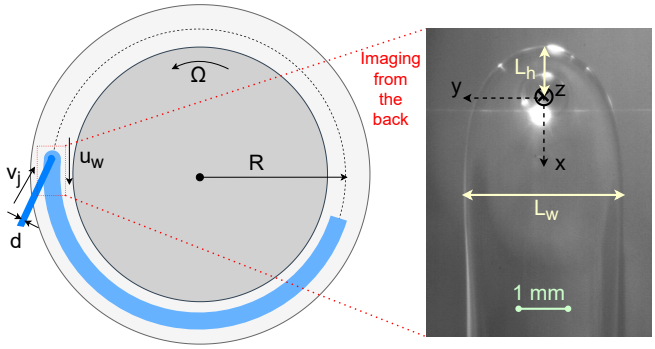


FIG. 1: Sketch of the experimental arrangement and an image from a typical experiment taken through the transparent polycarbonate disk.

The rotational speed of the disk is set using the variable frequency drive (VFD) on an electric motor. The VFD motor can drive the disk at an angular velocity $\Omega$ ranging from 50 to 2000 RPM, giving a local surface speed of 0.94 to 63 m/s at the impingement point, which lies at a radius of $R = 30$ cm from the centre of the disk. The rotational speed is measured using a digital hand-held tachometer (Fisher Scientific model No.0502824) with uncertainty of $\pm 1$ RPM.

For each experiment, the accumulator is first charged with test liquid and then pressurized to a set value by means of a compressed air cylinder and regulator. A solenoid valve is then opened to allow the liquid through the nozzle. To avoid any initial transients, the jet is initially redirected away from the disk by means of a deflector; 1.5 s after the solenoid valve is opened, the deflector is retracted and the jet is allowed to impinge on the spinning disk. Simultaneously, high speed cameras record the impingement process and a WIKA type A-10 pressure transducer behind the nozzle records the back pressure. The solenoid valve closes after the jet has impinged on the disk for one revolution. Following each test, a water jet is used to clean any liquid from the disk, which is then dried with a microfiber cloth.

Two interchangeable disks, 63 cm in diameter and 1.5 cm in thickness, are used. One disk is made of polished steel with a surface roughness of 1.8 $\mu$m on one half, and a mirror finish with surface roughness of 0.17 $\mu$m on the other half. The second disk is transparent and made of polycarbonate with a surface roughness of 0.13 $\mu$m. These arithmetic mean roughness values are measured by scanning a $0.5 \times 0.5\text{mm}^2$ sample surface with an Olympus LEXT OLS3100 confocal microscope. Switching the disks allows for testing on different surfaces and imaging from different angles. In particular the transparent disk allows imaging through the disk to determine the entire footprint of the lamella and its profile using laser induced fluorescence (LIF), as described below.

The nozzle assembly includes one of three interchangeable nozzle tips, with orifice diameters of $d_o = 810,\ 890,\ 1320\ \mu$m, that generate liquid jets of diameters $d = 760,\ 830,\ 1230\ \mu$m, respectively, as measured optically. These jet diameters are independent of the tested fluid and nozzle back pressure, presumably because the jet Reynolds numbers are sufficiently high that the vena contracta is constant. The jet velocity $v_j$ ranges from 2.6 m/s to 21 m/s. Further information about the nozzles and jets is provided in Ref. 15, including the calibration curves between nozzle back pressure and flow rate. The nozzle is positioned 5 cm away normal to the disk surface and is orientated such that the jet impinges almost perpendicularly (with an error of less than $4^\circ$ due to gravity).

For the steel disk, two high speed cameras (a Phantom V611 and a Phantom V7) record the jet impingement behavior and the lamella simultaneously from different angles. One camera is located slightly upstream from the jet and is orientated towards the impingement location; the optical axis of the second camera is orientated about $10^\circ$ relative to the disk surface to view the impingement region from the side. A high intensity 6700 Lumen white LED array with collimating lens illuminates the impingement area. The cameras record images at 1280 px$\times$800 px resolution, with typical magnifications corresponding with 20 $\mu$m/pixel, as determined by imaging a precision laser-engraved ruler.

For the transparent polycarbonate disk, a single high speed camera is located on the backside of the transparent disk, orientated along the axis of the jet. Fig. 1 shows a typical back-view image and highlights the local Cartesian coordinate system that we use to describe the geometry along with some key length measurements: $L_h$ and $L_w$. The heel length $L_h$ is defined as the distance from the center of the jet to the upstream edge of the liquid lamella in the $-x$ direction. The lamella width $L_w$ is defined as the widest portion of the lamella in the $y-$direction.

The three different mixtures of water and glycerol in Table I serve as Newtonian test liquids. Their fluid density $\rho$ is measured gravimetrically, and their viscosity $\mu$ is determined with an Anton-Paar Physica Modular Compact Rheometer 301. The measured density and viscosity are, respectively, within 0.5% and 3% of those reported elsewhere[31].

TABLE I: The composition and properties of test liquids at 23 °C .

| Glycerol concentration (wt%) | Viscosity (mPa · s) | Density (kg/m$^3$) |
|---|---|---|
| 70 | 19.4 | 1180 |
| 80 | 50.7 | 1197 |
| 85 | 91.5 | 1215 |

## B. Numerical Method

Three-dimensional simulations of a liquid jet impingement on a moving wall are conducted with ANSYS Fluent (2019 R3 release). In this code, the coupling between pressure $p(x,y,z,t)$ and velocity $\mathbf{u}(x,y,z,t)$ is achieved with the SIMPLE algorithm, spatial discretization is implemented through a second-order upwind scheme, and time discretization uses a first-order implicit scheme.

The interface between the liquid of the impacting jet and the surrounding air is tracked with the Volume of Fluid method (VOF)[32]. In VOF, the phase in each computational cell is represented by the liquid volume fraction, $\alpha(x,y,z,t)$, where $0 \leq \alpha \leq 1$ in any cell. A cell containing only liquid corresponds to $\alpha = 1$, and $\alpha = 0$ represents a cell filled with air; intermediate values of $\alpha$ indicate a cell that contains the interface. The liquid volume fraction is advected with local fluid velocity $\mathbf{u}$, and the material properties in a cell are determined by linear interpolation: $\rho = (1-\alpha)\rho_{air} + \alpha\rho_l$ and $\mu = (1-\alpha)\mu_{air} + \alpha\mu_l$. Practically, we adopt values for the density and viscosity of the liquid phase to match the experiments, taking those of the other phase to be characteristic of air at room temperature. For the bulk of the simulations (all results reported in Chapter §III and §V), we omit both gravity and surface tension. However, in a small number of cases, we include them to either gauge their effect (see §II C) or to more carefully match physical conditions (§II D), the ANSYS software allowing the incorporation of surface tension through a suitably defined body force[33].

### 1. Computational domain and boundary conditions

The computational domain is a rectangular prism of size $20d \times 7d \times 4d$. Fig. 2 shows the domain geometry and the associated boundary conditions. The domain is symmetric along the $y = 0$ plane and extends $4d$ upstream and $16d$ downstream from the impingement point at the origin. A semicircular jet is injected from the top boundary in the $(-z)$-direction and the bottom wall moves in the $(+x)$-direction. For the parameter space of interest, this domain is large enough to capture the entire upstream (against the motion of the wall) and lateral spread of the lamella. The domain is also sufficiently large in the downstream direction that viscous forces bring the entire lamella to the wall speed before reaching the downstream boundary.

The boundary conditions are as follows: along $y = 0$, symmetry conditions are applied. The moving wall is no slip:

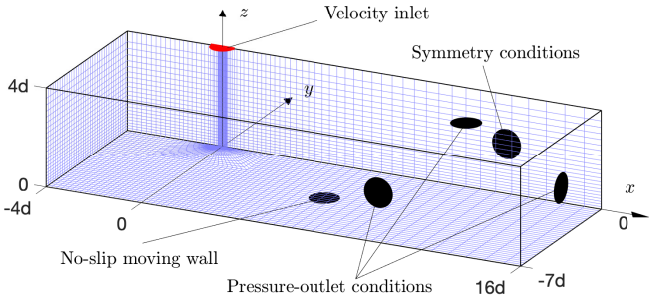


FIG. 2: Computational domain and associated boundary conditions. For clarity, the mesh shown is coarser than those used in the computations.

$\mathbf{u}(x,y,0,t) = (u_w,0,0)$. Over the semicircular region of the top boundary, $r = \sqrt{x^2+y^2} \leq d/2$ and $z = 4d$, the inflowing jet velocity and volume fraction are prescribed: $\mathbf{u}(x,y,4d,t) = (0,0,-v_j)^T$ and $\alpha(x,y,4d,t) = 1$. Along all other boundaries, pressure-outlet conditions are imposed, wherein the (gauge) pressure is set to be zero and all other conditions are extrapolated from the interior of the domain.

Computations are initiated with either no liquid from the jet in the domain, or using the final solution from an existing simulation with different parameter settings. The system of equations are then integrated forwards in time until a steady state is reached, or discontinued and rejected otherwise.

### 2. Meshing and mesh convergence

The computational domain is divided into cells using a non-uniform hexahedral mesh that is finer around the liquid jet (near $r = d/2$) and the lamella (near $z = 0$), while being coarser in areas that only contain air. Three grid resolutions are used, denoted as Coarse, Medium or Fine. For the Coarse grid, the mesh near the liquid jet forms an O-grid with $\Delta r = d/20$; the mesh gradually transitions to one of Cartesian-type and becomes fully Cartesian for $|x|, |y| \geq 2d$, with $\Delta x = \Delta y \approx d/10$ on $x < 2d$. In the downstream direction ($x > 2d$), $\Delta x$ gradually increases from cell to cell by a factor of 1.05. Along the $z$-direction, the mesh resolves the thin lamella: the cells adjacent to $z = 0$ have a vertical cell size $\Delta z = d/20$ and successive cell heights gradually coarsen by a factor of 1.03 with increasing $z$. An even coarser version of the grid is sketched in Fig. 2. The Coarse grid is refined once by halving the cell size in each dimension to obtain the Medium grid, and the Medium mesh is refined in the same fashion to achieve the Fine grid. Several cases are simulated with all three grids to study mesh convergence.

Before reporting the mesh convergence results, it is important to appreciate that there is an issue associated with the no-slip condition on the moving wall and our omission of any contact-line physics, which prevents the liquid from the jet from touching the moving plane. Instead, air unavoidably becomes swept along underneath the spreading liquid diverted from the jet. This air layer becomes too thin to resolve in the

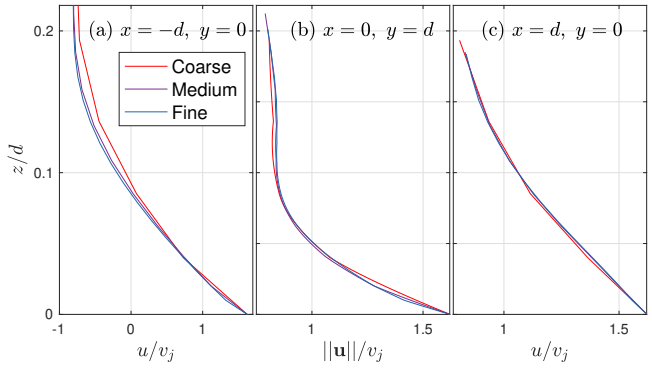


FIG. 3: Vertical profiles of horizontal velocity along three different vertical lines (as indicated) for the three grid resolutions, with $Re_j = 155$ and $u_w/v_j = 1.62$.

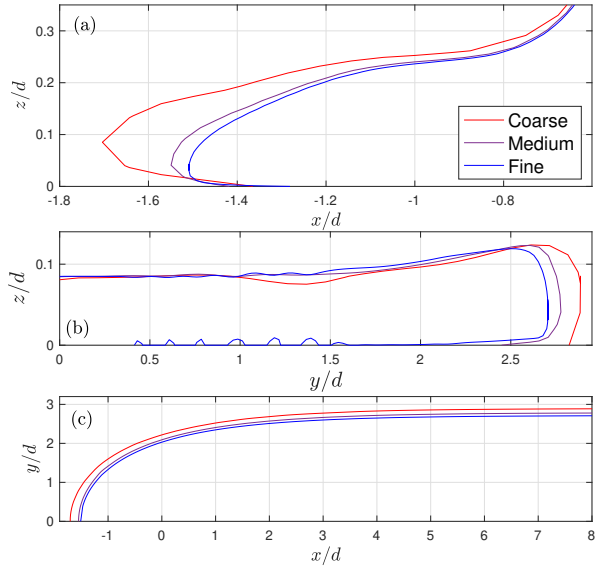


FIG. 4: Interface profiles for different grids with $Re_j = 155$ and $u_w/v_j = 1.62$, showing sections through (a) $y = 0$ and (b) $x = 8d$, then (a) the U-shaped footprint of the lamella on the $(x,y)-$plane. The vertical scale is exaggerated in (b).

computations, leaving an intermediate concentration within the lowest grid cells. The mesh refinement studies reported below indicate that the varying degree of resolution of the air layer does not appear to affect the convergence of the numerical solution elsewhere. The layer can also be artificially removed by suitably resetting the concentration field in the lowest grid cells. This device avoids any issues with spatial resolution, at the expense of an apparent violation of mass conservation, but again does not affect the solution elsewhere. Consequently, the unresolved air layer appears to be a minor price to pay for the the omisson of any contact-line physics. Nevertheless, numerical stability problems associated with the resolution failure become severe for lower velocity ratios, leading us to report results for only $u_w/v_j > 0.5$.

The benchmark case for which we report mesh convergence studies adopts the parameter values $Re_j = 155$ and $u_w/v_j = 1.62$. For the steady state reached in these computations, we compute the Grid Convergence Index[34] (GCI) for a few physical quantities of interest. Between the medium and fine grids, the *GCI* values for the heel length $L_h$ and lamella width $L_w$ are 2.66% and 1.51%, respectively. For the velocity profiles along select vertical lines shown in Fig. 3, the same *GCI* does not exceed 1%. We further observe that the *GCI* between the coarse and medium grids is about four times that between the medium and fine grids, indicating that the asymptotic range of convergence is achieved with these meshes (given an order of convergence of 2).

The air-liquid interface, identified by the surface where $\alpha = 0.5$, is plotted in Fig. 4 for the benchmark solutions on the three meshes. The first two panels show the convergence with refinement along sections through the heel and the downstream lamella at $x = 8d$. The air layer underneath the spreading liquid is visible in the latter, particularly for the fine mesh where the layer appears to break up into a series of distinctive "bubbles." The bottom panel shows the U-shaped footprint of the lamella, again demonstrating convergence with mesh refinement.

We conclude that mesh convergence is satisfactory from the Medium to the Fine mesh. The simulations in the following sections use the Medium mesh (where $\Delta z = d/40$) to achieve a balance between computational resources and accuracy. In a few cases where the lamella becomes very thin, the Medium mesh is further refined in the $z$ direction such that $\Delta z = d/80$ and that in all the cases there are at least 4 layers of cells across the thinnest part of the lamella. Even when the resolution becomes this poor, it arises well downstream where there is little structure to the velocity field.

### C. Dimensionless groups and confounding effects

A translation of the working dimensional parameters to Reynolds number and velocity ratio indicates that the experiments are conducted over the range,

$$15 \le Re_j = \frac{\rho v_j d}{\mu} \le 13000 \quad \text{and} \quad 0.04 \le \frac{u_w}{v_j} \le 14.$$

If $\sigma$ and $g$ denote surface tension and gravity, we further estimate that the Weber number, $We = \rho v_j^2 d/\sigma > 10$ (taking $\sigma = 0.64$ N/m), and Froude number, $Fr = u_w/\sqrt{gd} > 20$. These relatively high values imply that the effects of surface tension and gravity are less significant.

To explore the effect of surface tension in more detail, we conducted separate simulations in which we set $\sigma = 0.64$ N/m. Except for prompting a modest amount of capillary retraction further downstream, these additional computations suggested that interfacial effects at the air-water interface did not significantly impact the lamella dimensions. The capillary retraction, arising for Capillary numbers of $Ca_w = \mu u_w/\sigma < 18$, builds up an elevated ridge at the lamella's sides, and causes the maximum width to arise nearer the jet. Both effects can also be visually observed in the experiments (with

the retraction arising over distances comparable to the curvature from disk rotation). The simulations indicate that surface tension may reduce $L_w$ by up to 5%.

More awkwardly, the Froude number $Fr = u_w/\sqrt{gd} > 20$ estimates gravitational effects over distances of the jet diameter $d$, whereas the typical span of the lamella over the vertical surface of the disk is much greater. Nevertheless, even if we replace the jet diameter by a typical lamella length (which may be as much as $10d$) in the Froude number, this dimensionless estimator of gravitational effects still remains six or more. Thus, although it is possible that gravity may begin to affect the largest lamellas, it is unlikely to play a key role. To further gauge the importance of gravity, we conducted additional simulations in which gravity was included for a case with a relatively large lamella ($Re_j = 525$ and $u_w/v_j = 0.5$). In particular, simulations were conducted including gravity, orientating its direction in first the positive, and then the negative $x$ direction. These simulations, along with the corresponding simulation omitting gravity altogether, displayed no significant difference in lamella geometry.

The circular, rotating geometry of the spinning disk also does not reproduce the rectilinear motion of our target model problem. A measure of the effect of the Coriolis force experienced on the spinning disk is provided by the Rossby number,

$$Ro = \frac{u_w}{2d\Omega} = \frac{R}{2d} \sim \frac{0.3}{0.001} \sim 300. \qquad (1)$$

Since $Ro \gg 1$, the effect of the Coriolis forces should be negligible. In fact, to within experimental error, the lamella dimensions match between jet impaction on the spinning disk and on a surface moving rectilinearly (a belt sander), for a few select experimental parameters settings (jet speed, wall speed, jet diameter, etc.). Thus, the departure from rectilinear surface motion is not important in our spinning disk experiments.

Finally, the experimental lamella appears to be independent of the surface properties of the spinning disk: to within typical experimental errors, the dimensions $L_h$ and $L_w$ for experiments on the mirror-finished surface of the metal disk are the same as those on either the rougher surface or the polycarbonate disk. In other words, the corresponding surface roughnesses have no impact on the lamella geometry, consistent with the fact that flow is laminar and the characteristic roughness height ($0.17\ \mu\text{m} - 1.8\ \mu\text{m}$) is rather smaller than the lamella thickness.

### D. Detailed comparison

Table II compares the dimensionless heel length $L_h/d$ and lamella width $L_w/d$ from five experiments with results from simulations. The presented values for the simulations are Richardson extrapolations[35], based on results computed with the Medium and Fine grids. The five cases span a range of operating parameters, all of which are matched in the simulations, including surface tension and gravity towards the $x$-direction. Except in a single case, the differences between the simulations and experiments are less than 10%; the CFD mostly predicts larger lamella dimensions.

## III. PHENOMENOLOGY

### A. Regime Diagram

Fig. 5 shows the observed behaviour on the steel disk with the mirror surface. Three regimes are identified: steady deposition, unsteady splashing, and a transitional regime between the two. For steady deposition, the jet spreads out smoothly to form a distinctive, U-shaped lamella, as reported previously and shown earlier in Fig. 1. During unsteady splashing, the edge of the heel lifts up, then fragments to release small droplets (see the snapshot of Fig. 6(a)). Over the transitional regime, the flow alternates irregularly between smooth deposition and splashing, as found by Keshavarz et al.[26]. At much higher Reynolds numbers, beyond the limits of the plot in Fig. 5, the jet itself becomes turbulent and we have observed bubbly turbulent bores upstream of the jet, as illustrated in Fig. 6(b) for an experiment conducted using water (*cf.* 25).

The transition between steady deposition and splashing largely follows a contour of constant $Re_j(1 + u_w/v_j)$ (see Fig 5). Because splashing arises when the heel lifts up, this observation is consistent with the hypothesis, following classical arguments for drop impacts[36], that the transition occurs when the velocity difference between the fluid and the underlying surface (which is $u_w + v_j$ for the heel) reaches a critical threshold, holding the properties of the ambient air and surface tension fixed (see also Ref. 37). As this threshold is likely sensitive to the surface properties of the disk and ambient air properties[28], we have not tried to quantify the transition any further experimentally; the regime diagram in Fig. 5 applies only to the mirrored steel disk at standard atmospheric pressure. We also avoided any detailed exploration of the transition using the numerical simulations, as the solutions did not remain trustworthy when the dynamics become unsteady and suggestive of splashing at higher Reynolds numbers and velocity ratios.

### B. Steady lamellae

Our main focus is on the regime of steady deposition; Fig. 7 presents a collage of images showing how the lamella structure varies as the operating parameters sweep across this area of the regime diagram. A similar collection of interface profiles from the simulations is shown in Fig. 8. Both figures indicate that the lamella dimensions $L_h$ and $L_w$ increase when $Re_j$ increases, or as $u_w/v_j$ decreases.

For most of the regime (approximately $15 < Re_j < 400$ and $0.3 < u_w/v_j < 3$), a steady heel forms upstream from the impingement point, and the liquid spreads into a lamella of nearly constant lateral width. Examples of this behaviour may be seen in the middle columns of Figs. 7 and 8 (see also Fig. 4). To the upper left-hand part of the deposition regime (approximately $Re_j > 200$ and $u_w/v_j < 0.3$), the heel develops an elevated rim, as observed for the top-left case ($Re_j = 200, u_w/v_j = 0.3$) in Fig. 7. For the simulations, similar features also appear, although sometimes taking the form

TABLE II: Experimental (Exp) results compared with simulation (CFD) results with matching operating parameters.

| $Re_j$ | $u_w/v_j$ | $L_h/d$ (Exp) | $L_h/d$ (CFD) | Rel. Err. (%) | $L_w/d$ (Exp) | $L_w/d$ (CFD) | Rel. Err. (%) |
|---|---|---|---|---|---|---|---|
| 16 | 1.06 | 0.89±0.06 | 0.87±0.01 | -2 | 2.80±0.14 | 2.61±0.01 | -7 |
| 73 | 0.84 | 1.34±0.06 | 1.56±0.01 | 16 | 4.63±0.14 | 5.34±0.05 | 15 |
| 159 | 0.96 | 1.83±0.06 | 1.84±0.01 | 1 | 6.05±0.14 | 6.51±0.03 | 8 |
| 158 | 2.89 | 1.10±0.06 | 1.11±0.01 | 1 | 3.47±0.14 | 3.60±0.03 | 4 |
| 208 | 2.71 | 1.24±0.06 | 1.25±0.01 | 1 | 3.85±0.14 | 4.19±0.08 | 9 |
| 296 | 1.03 | 2.15±0.06 | 2.30±0.01 | 7 | 7.14±0.14 | 7.66±0.02 | 7 |

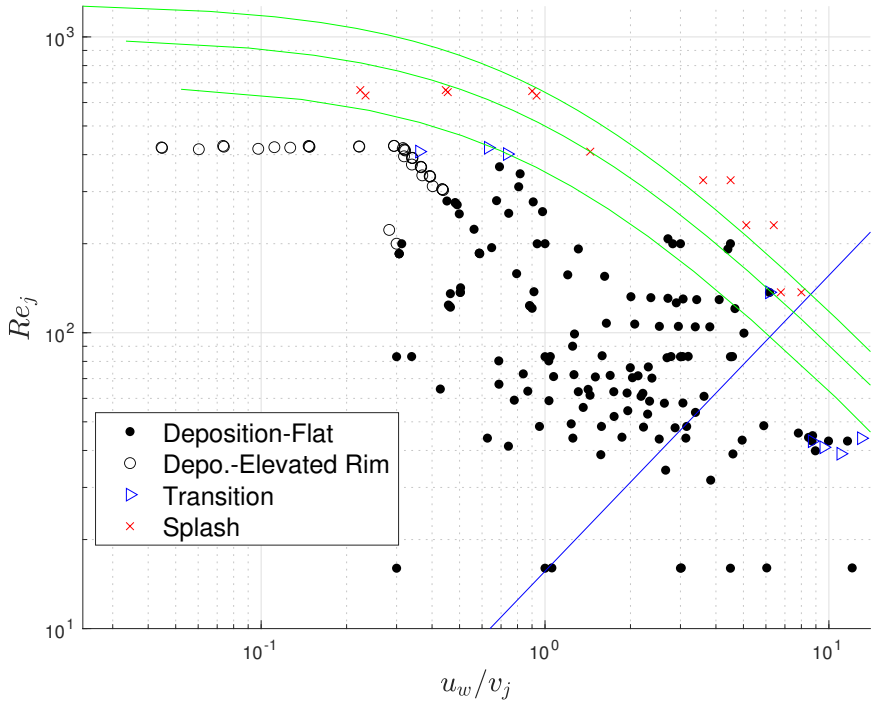


FIG. 5: Experimental regime diagram. The different regimes are described in the text. The blue line marks $[Re_j/(u_w/v_j)]^{1/3} = 2.5$ (see §V). The green lines show the contours $(1+u_w/v_j)Re_j = 700, 1000, 1300$.

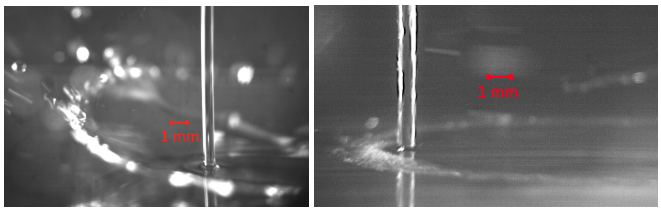


FIG. 6: Examples of (a) a splash at $Re_j = 619$, $u_w/v_j = 0.44$, and (b) a turbulent bore at $Re_j = 5840$, $u_w/v_j = 0.3$.

of a stationary wavetrain (Fig. 8, top left). Finally, below the blue line marked in Fig. 5 (which is rationalized in §V below), the heel becomes relatively small, or even disappears, and the lamella width approaches the jet diameter (lower right cases in Figs. 7 and 8).

### C. Lamella anatomy

Based upon the classical discussions of jet impact onto stationary walls, one expects the lamella to decompose into a number of distinct regions with different dynamical character. First, given the relatively high jet Reynolds number, the incoming fluid is expected to be diverted into a radially outgoing potential flow by high impact pressures. Second, outside the impact zone, viscous stresses grow in importance, gradually encroaching on the outflow from below and redirecting fluid motion into the direction of the wall, thereby forming the upstream heel. Unlike the traditional impingment problem in which the potential flow sits directly above a stationary wall, this viscous redirection also implies that a layer of liquid must be carried back underneath the jet from the heel, cushioning the impact. Last, far downstream (for $x$ of $O(L_h)$), the lamella must approach constant width once all the fluid

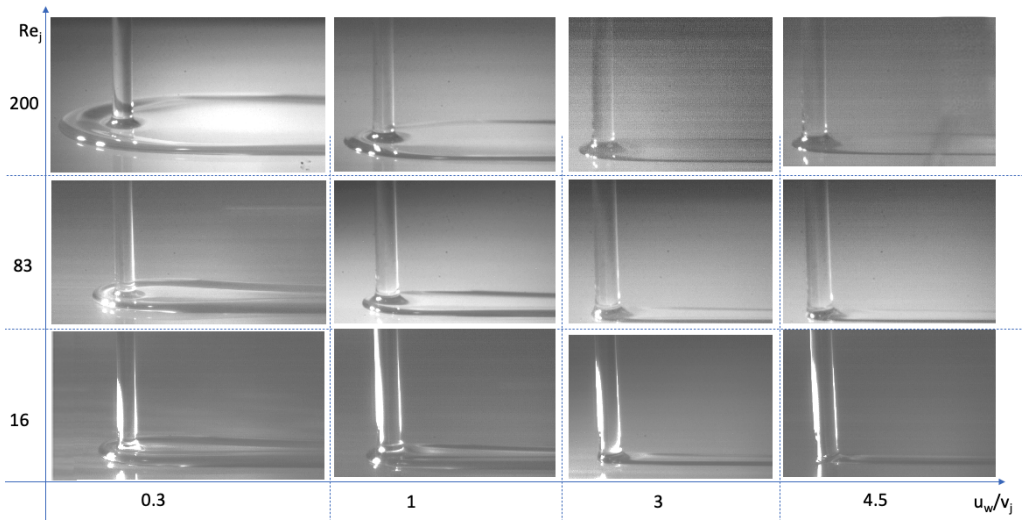


FIG. 7: Experimental lamella shapes at varying $Re_j$ and $u_w/v_j$. The slight tilt of the jet in some images is caused by gravity as the jet impinges horizontally. The tilt is less than $4^\circ$, and the perpendicular velocity component is below 0.2% of $v_j$.

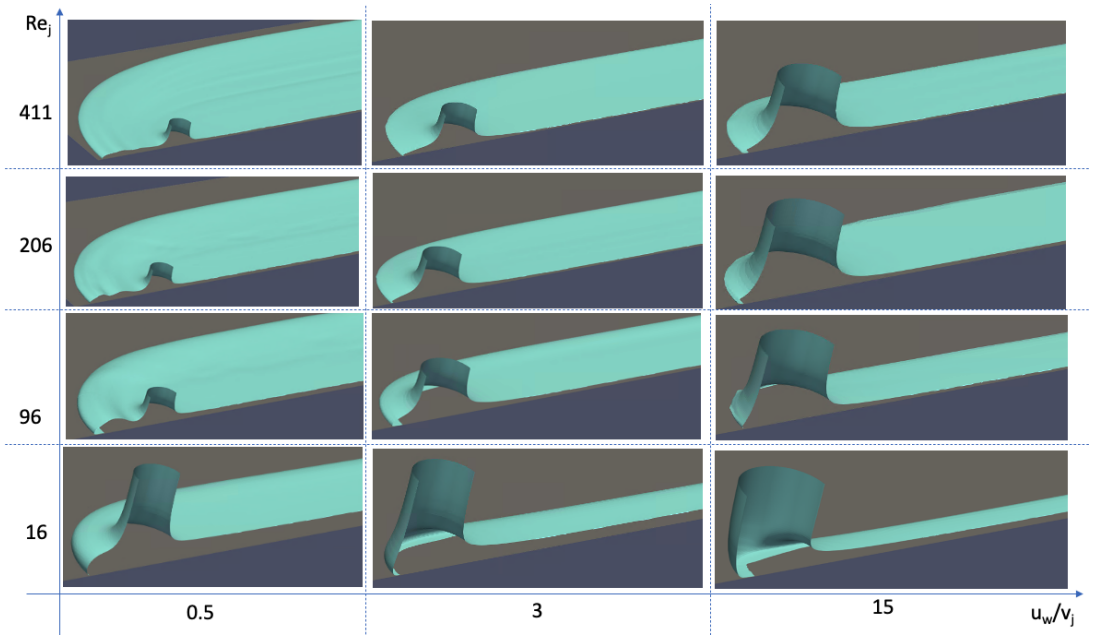


FIG. 8: Simulated lamella shapes for varying $Re_j$ and $u_w/v_j$.

reaches the wall speed $u_w$. Mass balance at this stage sets the average thickness of the lamellar $\overline{h}$ in terms of its width $L_W$: $\overline{h} = \pi d^2 v_j/(4u_w L_w)$.

To confirm these expectations, we select three examples with varying velocity ratio, $u_w/v_j$, but fixed jet Reynolds number $Re_j = 137$. These examples are presented in Figs. 9-11, and correspond to cases with lamellae that are relatively wide, typical and narrow, respectively. Cuts through the impact pressure distribution that diverts the jet are shown along the top row, scaled by $\frac{1}{2}\rho v_j^2$. High pressure is restricted to the region directly underneath the jet, falling quickly to ambient values beyond. In the inviscid jet impingement problem for a stationary wall,[3,4] elevated pressures arise over an impact zone with $r = \sqrt{x^2+y^2} < d$. As seen in Figs. 9-11, the extent of the impact zone is similar for a viscous jet impinging on a moving wall, although in the example with the fastest wall speed (Figs. 11), the upstream diverted fluid is redirected downstream before reaching such radii.

Streamlines drawn over the top surface of the lamella (lower left panels) display the viscous redirection more clearly: upstream of the jet axis ($x < 0$), a fraction of the fluid elements within this surface turn and become tangential to the edge of the lamella before proceeding underneath to create the underlying return flow (see also the streamlines drawn in the midplane $y = 0$ in panels (e)). The other streamlines remain on the top surface and turn more gradually to the wall direction.

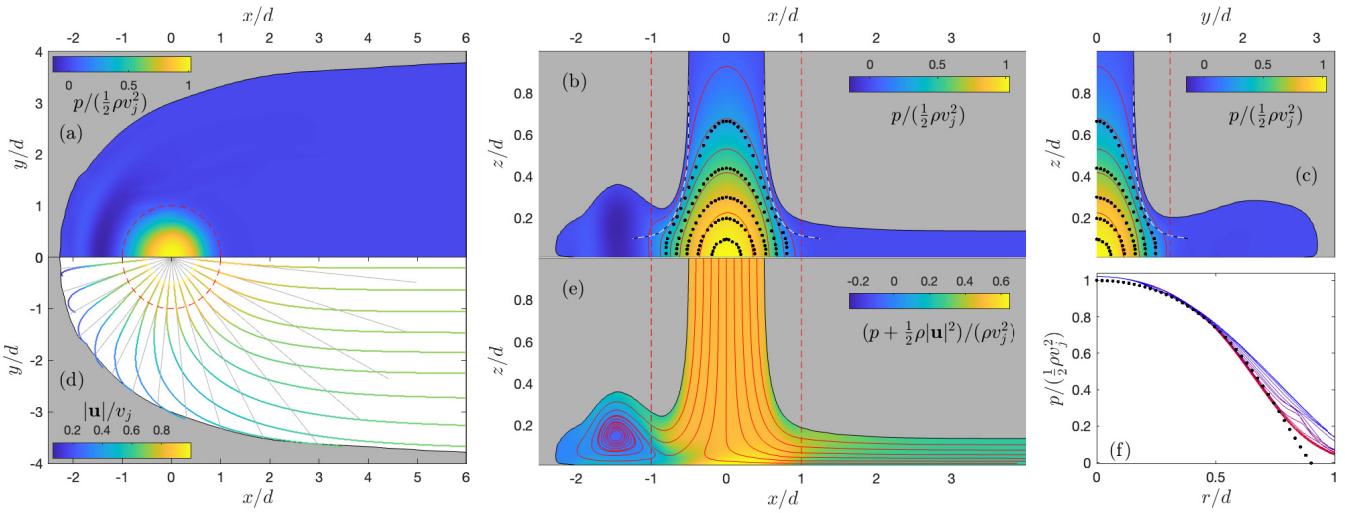


FIG. 9: Simulation results for $Re_j = 137$ and $u_w/v_y = 0.7$. The pressure distribution is plotted along the top row, for (a) $z = 0.04d$, (b) $y = 0$ and (c) $x = 0$. The black dots show select contours of constant pressure for the inviscid solution of Lienhard et al.[3,4]; the corresponding contours from the simulation are indicated by the red lines. Lienhard et al.'s interface profile is plotted by the black and white dashed line. The lower row displays (d) streamlines along the top surface, (e) the distribution of the Bernoulli function $p + \frac{1}{2}\rho|\mathbf{u}|^2$ for $x = 0$, and (f) radial pressure distributions along $z = 0.04d$ and the angular cuts shown in (d). The streamlines of (d) start at $r = \frac{1}{2}d$ and $z = \frac{3}{2}d$, and are coloured according to the local speed $|\mathbf{u}|$. In (e), the red lines indicate a selection of streamlines beginning at $z = \frac{3}{2}d$. The black dots in (f) show Lienhard et al.'s inviscid pressure solution and the curves are colour coded, from $\theta = 0$ (red) to $\theta = \pi$ (blue). The red dashed lines indicate $r = d$, and the vertical scale in (b,c,e) is exaggerated.

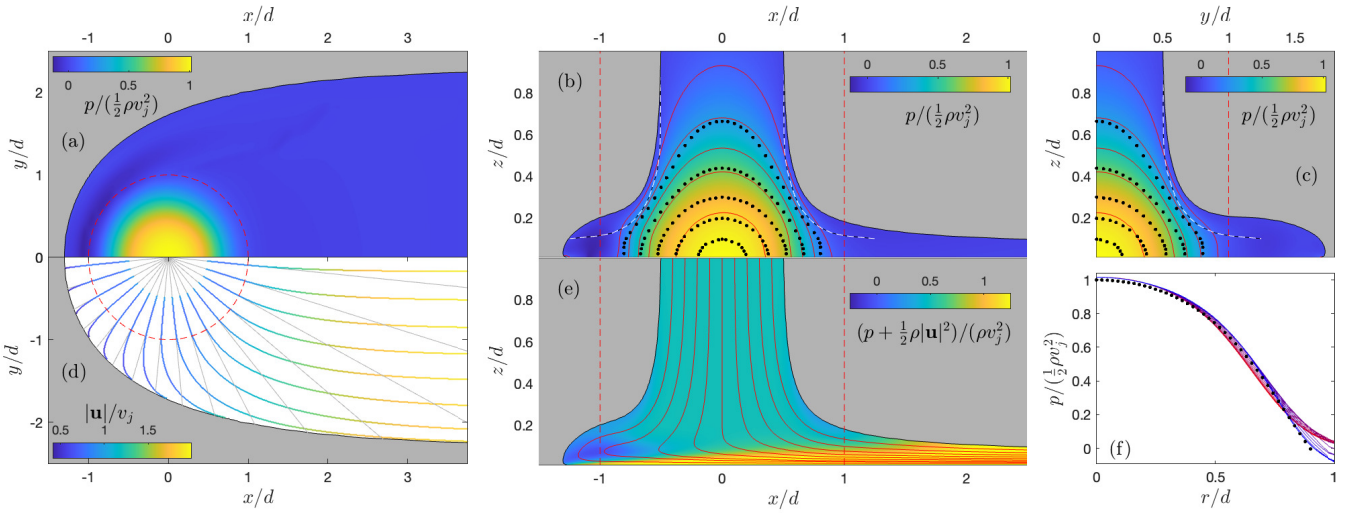


FIG. 10: A similar set of plots to those in figure 9, but for $u_w/v_j = 2$.

In all three cases, the radial pathways taken by the diverted fluid from the jet extend, at most, only a little way beyond the impact zone ($r < d$).

To visualize the diverted potential flow from the jet, we plot, in the middle lower panels of Figs. 9-11, the Bernoulli function, $p + \frac{1}{2}\rho|\mathbf{u}|^2$, over the midplane $y = 0$. This quantity is largely constant for the potential flow region, but changes as viscous redirection takes effect. For the example with lowest wall speed, the interface develops a prominent bump upstream of the jet, as seen earlier in Fig. 8. This bump corresponds to a recirculation cell (Fig. 9(e)), which traps fluid elements lying perfectly in the midplane; neighbouring elements to either side spiral through and then out of the cell. The sections through the midplane $y = 0$ have some similarity with the flow patterns seen for planar jets impacting a moving wall[14,15], even though the geometrical constraints of that two-dimensional problem are very different.

Figs. 9-11 also shows the inviscid interface position and

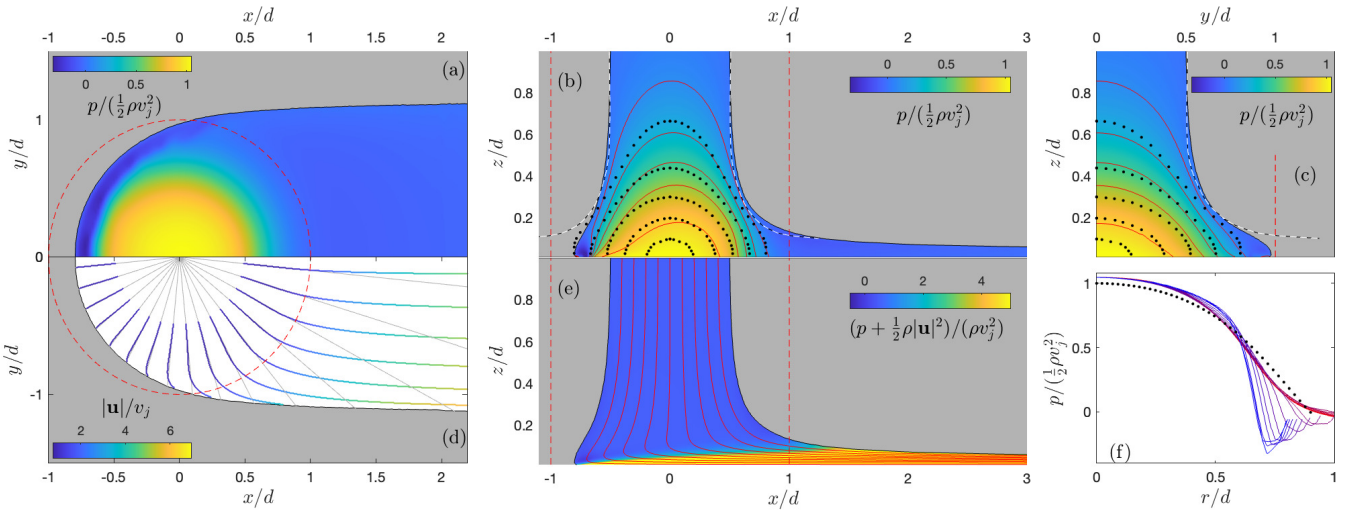


FIG. 11: A similar set of plots to those in figure 9, but for $u_w/v_j = 7$.

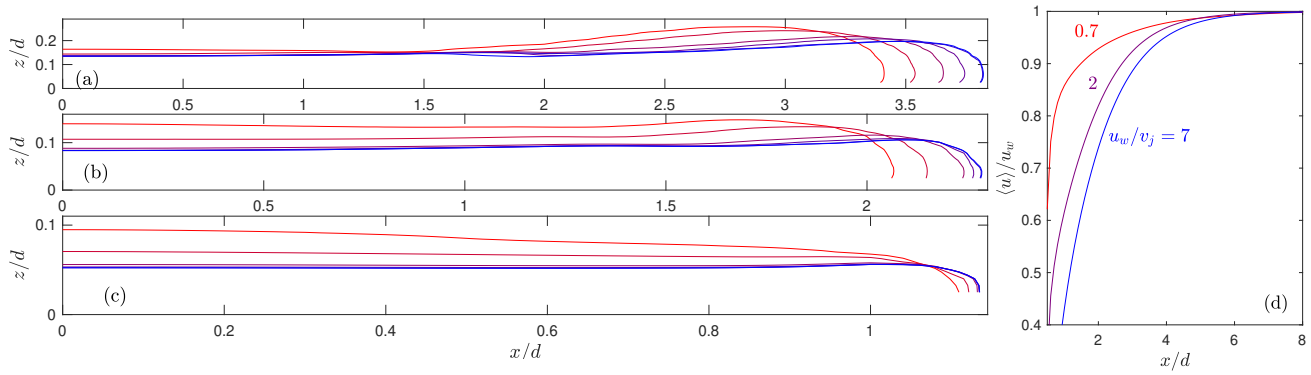


FIG. 12: Sections through the upper interface of the lamella at $x = \frac{4}{3}d$, $2d$, $\frac{7}{2}d$, $5d$, $8d$ and $14d$ (from red to blue) for simulation with (a) $u_w/v_j = 0.7$, (b) $u_w/v_j = 2$, and (c) $u_w/v_j = 7$; $Re_j = 137$. The convergence of the downstream speed $\langle u\rangle/u_w$, averaged over the liquid phase and scaled by $u_w$, for all three cases is shown in (d).

pressure distribution presented by Lienhard et al.[3,4]. In their solution, the decay of the impact pressure for $r \to d$ implies that the fluid diverted from the jet creates a radially outgoing film of thickness $h = \frac{1}{8}d$ there (the incoming volume flux $\frac{1}{4}\pi d^2 v_j$ corresponds to an outgoing flux of $2\pi d h v_j$). The local depths near the edge of the impact zones in the numerical simulations are somewhat deeper as a result of the underlying return flow. Although the return flow also distorts local pressures, the impact pressure distribution remains close to Lienhard et al.'s solution near the moving wall (panels (f)). Higher up within the impact zone (panels (b,c)), the comparison degrades.

The approach to the final downstream lamella profile for the three examples is shown in more detail in Fig. 12. The left-hand panels display a sequence of sections through the lamella at fixed downstream stations, $x$. These highlight the perhaps surprising feature that the bulk of the final profile has a uniform depth. The convergence of the average downstream speed $\langle u\rangle$ (with the average taken over the liquid phase) to the wall speed is shown in panel (d); evidently, the fluid reaches this state well before travelling distances of order $10d$.

## IV. A MODEL FOR THE LAMELLA U-SHAPE

To provide a simple model of the U-shape of the lamella, we use a relatively simple argument inspired by one proposed by Wilson et al. for the cleaning of a soiled surface by a moving jet[38]. To begin, we first observe that the U-shape is determined mostly outside the impact zone, where the outflow from the jet appears much like a point source with constant flux $Q = \frac{1}{4}\pi d^2 v_j$. As discussed by Watson[5], if there were no motion of the wall, the radial velocity of this outflow would then be approximately given by the boundary-layer form,

$$u(r,z) = U(r) f(\eta), \quad \eta = \frac{z}{h(r)},$$

where $h(r)$ is the local depth, the profile function $f(\eta)$ satisfies the conditions, $f(0) = f'(1) = 0$ and $f(1) = 1$, and the

radial velocity on the top surface is

$$U(r)=\frac{A}{r^3},\quad A=\frac{c\rho_l Q^2}{\mu},\quad c=\frac{3\int_0^1 f^2 \mathrm{d}\eta}{4\pi^2 f'(0)(\int_0^1 f\mathrm{d}\eta)^2}. \quad (2)$$

For the similarity solution used by Watson for $f(\eta)$, the constant $c=0.0681$; the simpler quadratic profile $f(\eta)=\eta(2-\eta)$, often used with the von Karman-Pohlhausen integral averaging method, yields instead $c=0.0456$.

In our Cartesian coordinates centered at the jet, the superposition of the free-surface velocity with the uniform wall speed is

$$\begin{pmatrix} u_w+U\cos\theta \\ U\sin\theta \end{pmatrix}, \quad (3)$$

where $\theta$ is the polar angle. We now parameterize the edge of the lamella by $r=r(\theta)$. If this curve is set by the condition that the velocity field in (3) has no normal component along $r=r(\theta)$, then

$$(r'\sin\theta+r\cos\theta, r\sin\theta-r'\cos\theta)\cdot\begin{pmatrix} u_w+U\cos\theta \\ U\sin\theta \end{pmatrix}=0.$$

With the form of $U(r)$ given by Eq. (2), we now arrive at

$$\frac{\mathrm{d}}{\mathrm{d}\theta}[(r\sin\theta)^3]=-\frac{3A}{u_w}(\sin\theta)^2. \quad (4)$$

Thus, if $y\equiv r\sin\theta=0$ at $\theta=\pi$,

$$y^3=r^3\sin^3\theta=\frac{3A}{u_w}\int_\theta^\pi \sin^2\theta\mathrm{d}\theta.=\frac{3A}{4u_w}(2\pi-2\theta+\sin 2\theta). \quad (5)$$

Consequently,

$$r(\theta)=L_h\left[\frac{3(2\pi-2\theta+\sin 2\theta)}{4\sin^3\theta}\right]^{\frac{1}{3}} \quad (6)$$

and

$$L_h=\left(\frac{A}{u_w}\right)^{\frac{1}{3}}, \quad (7)$$

given that $[(2\pi-2\theta+\sin 2\theta)/\sin^3\theta]\to\frac{4}{3}$ and $r\to L_h$ for $\theta\to\pi$. In view of (2), the heel lengh can be written as

$$\frac{L_h}{d}=a\cdot Re_j^{\frac{1}{3}}\cdot\left(\frac{v_j}{u_w}\right)^{\frac{1}{3}}, \quad (8)$$

where $a=0.45$ for Watson's similarity solution and $a=0.30$ for the quadratic boundary layer profile.

Finally, taking the limit $\theta\to 0$ in Eq. (5) now furnishes the lamella half-width,

$$L_w=2y|_{\theta=0}=2\left(\frac{3\pi}{2}\right)^{\frac{1}{3}}L_h\approx 3.35L_h. \quad (9)$$

Therefore, both the heel length $L_h$ and the lamella width $L_w$ follow the same dependence on $Re_j$ and $(u_w/v_j)$. The U-shape predicted by (6) has a somewhat similar form to the Rankine half body (Fig. 13), even though that latter shape is prescribed purely by potential flow. More importantly, the U-shape is predicted to adopt a universal form after scaling by the lamella width.

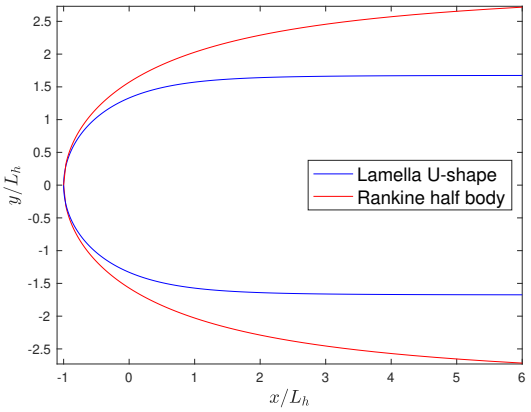


FIG. 13: The prediction for the steady lamella U-shape in Eqn. 6 compared with the Rankine half body, for which $r/L_h=(\pi-\theta)/\sin\theta$.

Note that the power-law dependence of $L_w$ and $L_h$ on Reynolds number and velocity ratio follow from much simpler scaling arguments characteristic of traditional boundary-layer theory: when the velocity is veering towards the wall speed within the lamella, the inertial terms in the momentum equation are $O(u_w^2/L_w)$. These must balance the viscous stress, which is of order $\mu u_w/(\rho\bar{h}^2)$. But $\bar{h}=O(v_j d^2/(u_w L_w))$ from the global mass balance. Hence, if $L_h=O(L_w)$, we observe that both must scale as $(u_w/v_j)^{-1/3}Re_j^{1/3}$.

## V. ANALYSIS

To interrogate the predictions of the simple model of §IV, we collect together data extracted from our experiments and simulations. Fig. 14 shows the (scaled) heel lengths and lamella widths, $L_h/d$ and $L_w/d$, for series of simulations and experiments with varying Reynolds number $Re_j$ at fixed velocity ratio $u_w/v_j$. Fig. 15 shows similar data, but for series with varying $u_w/v_j$ at fixed $Re_j$. Experimentally, it is difficult to control $v_j$ precisely in order to set $Re_j$ and $u_w/v_j$ for any one series of tests, so results with velocity ratios or Reynolds numbers within the bounds indicated in the legends are selected. In Fig. 14 both simulations and experiments suggest that $L_h$ and $L_w$ have a power-law dependence on Reynolds number with a power that is close to $\frac{1}{3}$, as predicted by Eqs. (8) and (9). The data in Fig. 15 is less suggestive of a power-law dependence on $u_w/v_j$ with an exponent predicted by Eqs. (8) and (9) (*i.e.* $-\frac{1}{3}$), and point to a potentially richer dependence on velocity ratio.

Fig. 16 presents the full set of experimental and numerical data for heel length $L_h$ and lamella width $L_w$. In the first two panels of this figure, guided by §IV, we formulate the scaled

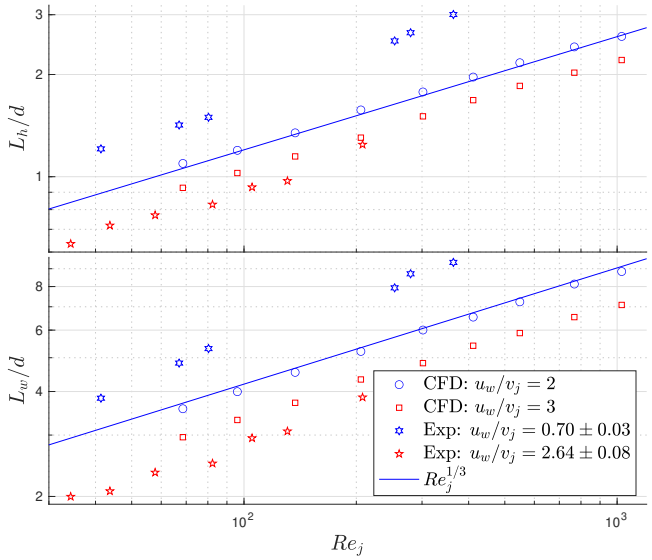


FIG. 14: Heel lengths (top) and lamella widths (bottom) for series of experiments ("Exp") and simulations ("CFD") with varying $Re_j$ at fixed $u_w/v_j$ (as indicated). The blue line indicates a power law of $1/3$.

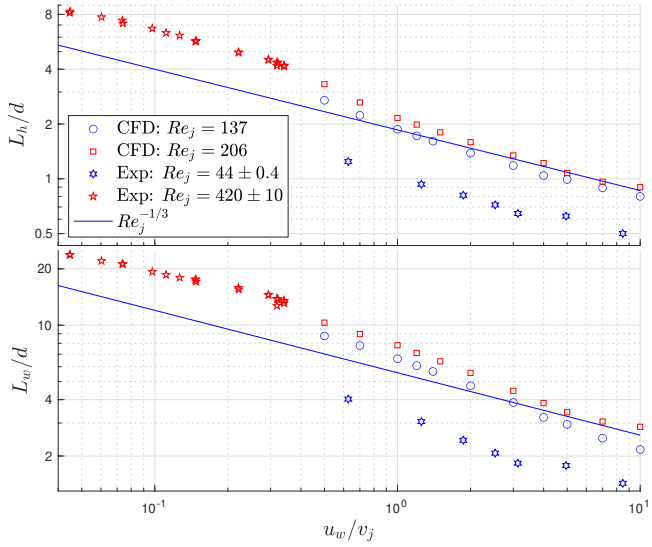


FIG. 15: Heel lengths (top) and lamella widths (bottom) for varying $u_w/v_j$ at fixed $Re_j$ (as indicated). The blue line indicates a power law of $-1/3$.

lengths,

$$\frac{L_h}{d}\left(\frac{u_w}{v_j Re_j}\right)^{\frac{1}{3}} \quad \text{and} \quad \frac{L_w}{d}\left(\frac{u_w}{12\pi v_j Re_j}\right)^{\frac{1}{3}}.$$

and plot them against $(Re_j v_j/u_w)^{1/3}$ to separate cases at different operating parameters. In the simple model, these scaled lengths equal a constant depending upon the boundary layer velocity profile. Specifically, the constant is 0.30 for the quadratic profile, indicated by the blue horizontal lines in Fig. 16, and 0.45 for Watson's similarity solution, shown by

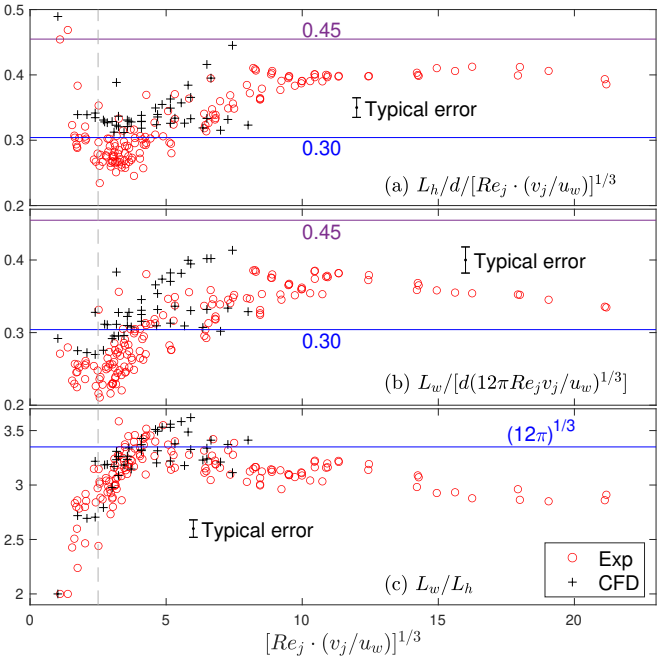


FIG. 16: Scaled heel lengths and lamella widths plotted against $Re_j(v_j/u_w)^{1/3}$ for both experiments and CFD. The horizontal lines show the values predicted by the simple model of §IV (using either Watson's similarity solution or the quadratic boundary-layer profile).

the purple line. The model also predicts that the ratio $L_w/L_h$ should equal the constant value $(12\pi)^{1/3}$; we plot this ratio against $(Re_j v_j/u_w)^{1/3}$ in Fig. 16(c).

Overall, the data from both the experiments and simulations are in broad agreement with the predictions of the simple model. For lower values of $(Re_j v_j/u_w)^{1/3}$, there is a suggestion in Fig. 16 of a trend away from a constant value, due perhaps to the fact that the heel length for these cases is relatively short. Indeed, if $L_h \le d$ in Eq. (8), or $[Re_j \cdot (v_j/u_w)]^{1/3} < a^{-1}$, the heel is predicted to occur within the impact zone. The diverted outflow cannot then appear to come from a point source. Accordingly, taking a value for $a$ midway between 0.30 and 0.45, we adopt the rough criterion,

$$[Re_j \cdot (v_j/u_w)]^{1/3} < \frac{5}{2}, \tag{10}$$

as an indicator for when the steady lamella has a heel that is too small to be described by the model. This limit is indicated by the vertical dashed line in Fig. 16, and is also displayed on the regime diagram in Fig. 5.

Finally, Fig 17 plots the horizontal footprints of lamella, scaled by $L_w$, for a collection of profiles from the experiments and simulations. The top panel shows scaled shapes for cases with varying $Re_j$ at fixed $u_w/v_j$; the bottom panel has fixed $Re_j$ and varying $u_w/v_j$. All the shapes are collapsed by the scaling, even though both $Re_j$ and $u_w/v_j$ vary by an order of magnitude, and all align satisfyingly with the curve given by Eq. (6).

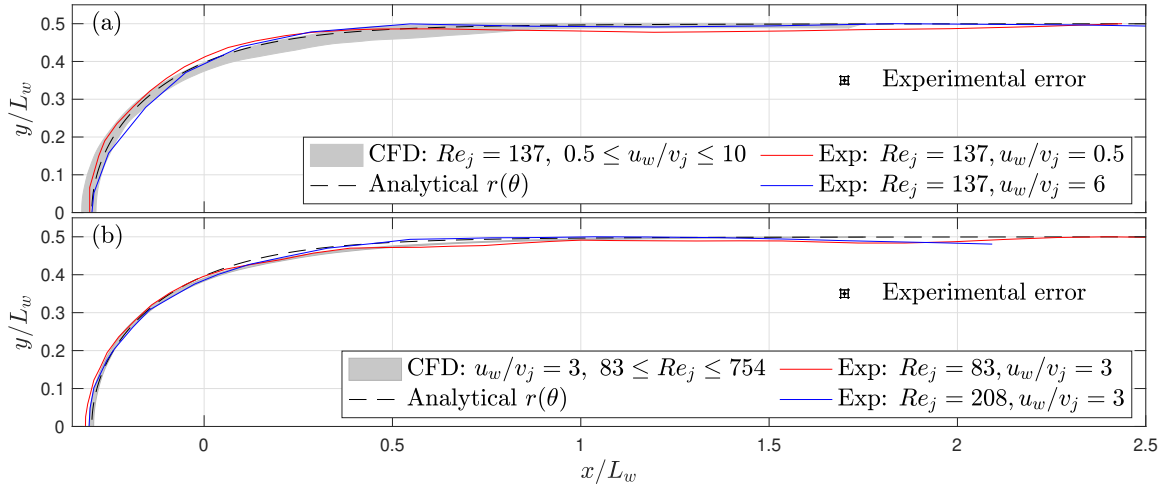


FIG. 17: Lamella shapes from experiments ("Exp") and simulations ("CFD") scaled by $L_w$ and compared with the prediction in Eq. (6), for (a) fixed $u_w/v_j$ and varying $Re_j$, and (b) fixed $Re_j$ and variable $u_w/v_j$. The shaded area shows the average (in polar coordinates), plus or minus the standard deviation of six simulations.

## VI. CONCLUSION

In this study, the impingement of a liquid jet on a dry moving wall has been studied using experiments and numerical simulation. At low values of $Re_j$ and high values of $u_w/v_j$, the impinging liquid jet becomes immediately dragged downstream by viscous stresses, forming a thin liquid stripe with a width given approximately by the jet diameter $d$. At high values of jet Reynolds number or wall speed, jet impingement prompts a splash. For an intermediate range of conditions, steady deposition results, with the liquid spreading into a U-shaped lamella. Experimentally, we collected such observations together and provided an empirical regime diagram on the $(Re_j, u_w/v_j)$-plane that identifies the steady deposition phase.

The numerical simulations enable a deeper examination of the structure of the lamella: high impact pressures divert the liquid jet sideways in a nearly potential-flow adjustment. Subsequently, a viscous deflection turns the fluid towards the direction of motion of the wall. This viscous redirection creates a distinctive heel upstream of the jet that returns fluid underneath the jet, cushioning its impact. After travelling distances of less than ten or so jet diameters, all the fluid is eventually brought to the wall speed. Surprisingly, the final fluid film has almost uniform depth.

Guided by this vision of lamella dynamics, we constructed a simple model for the shape of the lamella. This model predicts the length of the heel, the width of the downstream lamella, and that the entire shape adopts a characteristic universal form if scaled by one of these distances. Results from both the experiments and the simulations are in agreement with these predictions, except when the heel becomes relatively small.

There are a number of open questions and suggestions for future work arising from this study. The simple model for the lamella shape is relatively crude, yet works surprisingly well. The model does not, however, provide any insight into why the fluid surface eventually becomes flat. These mixed successes of the model motivate a more careful analysis. We have also devoted little attention to the transition to splashing that limits the deposition to one side of our regime diagram. Although there have been some experimental studies of the onset of splash for an impinging jet[26,27], there is currently no robust analytical model to provide complementary predictions. We also did not explore the impingement dynamics for very low velocity ratios. Here it is conceivable that the upstream heel becomes extended, forming an elevated rim that eventually develops into a hydraulic jump. Finally, our study applies to Newtonian fluids, but the relatively large range of strain rates occurring during impingemenmt, coupled with the wide range of applications with potentially complex fluids, suggest that an exploration of the non-Newtonian version of the problem would be worthwhile.

## ACKNOWLEDGMENTS

The financial support of Natural Sciences and Engineering Research Council of Canada (NSERC) is gratefully acknowledged. This research was undertaken, in part, thanks to funding from the Canada Research Chairs program.

## DATA AVAILABILITY STATEMENT

Data available on request from the authors.

[1] W. Schach, "Umlenkung eines freien Flüssigkeitsstrahles an einer ebenen Platte," Ingenieur-Archiv **5**, 245–265 (1934).
[2] T. Strand, "On the theory of normal ground impingement of axisymmetric jets in inviscid incompressible flow," in *1st Annual Meeting* (1964) p. 424.
[3] X. Liu, L. A. Gabour, and J. H. Lienhard, "Stagnation-Point Heat Transfer During Impingement of Laminar Liquid Jets: Analysis Including Surface Tension," Journal of Heat Transfer **115**, 99 (1993).

[4]J. H. Lienhard, "Heat transfer by impingement of circular free-surface liquid jets," in *18th National and 7th ISHMT-ASME, Heat and Mass Transfer Conference, Guwahati, India* (2006).
[5]E. Watson, "The radial spread of a liquid jet over a horizontal plane," Journal of Fluid Mechanics **20**, 481–499 (1964).
[6]R. Bowles and F. Smith, "The standing hydraulic jump: theory, computations and comparisons with experiments," Journal of Fluid Mechanics **242**, 145–168 (1992).
[7]F. Higuera, "The hydraulic jump in a viscous laminar flow," Journal of fluid Mechanics **274**, 69–92 (1994).
[8]T. Bohr, P. Dimon, and V. Putkaradze, "Shallow-water approach to the circular hydraulic jump," Journal of Fluid Mechanics **254**, 635–648 (1993).
[9]J. W. Bush and J. M. Aristoff, "The influence of surface tension on the circular hydraulic jump," Journal of Fluid Mechanics **489**, 229–238 (2003).
[10]R. Kate, P. Das, and S. Chakraborty, "Hydraulic jumps due to oblique impingement of circular liquid jets on a flat horizontal surface," Journal of Fluid Mechanics **573**, 247–263 (2007).
[11]D. Wilson, B. Le, H. Dao, K. Lai, K. Morison, and J. Davidson, "Surface flow and drainage films created by horizontal impinging liquid jets," Chemical engineering science **68**, 449–460 (2012).
[12]R. Bhagat and D. Wilson, "Flow in the thin film created by a coherent turbulent water jet impinging on a vertical wall," Chemical Engineering Science **152**, 606–623 (2016).
[13]R. K. Bhagat, N. Jha, P. Linden, and D. I. Wilson, "On the origin of the circular hydraulic jump in a thin liquid film," Journal of Fluid Mechanics **851** (2018).
[14]X. Liu, S. Green, B. Stoeber, and N. J. Balmforth, "Flow of a shallow film over a moving surface," Physics of Fluids **34**, 083602 (2022).
[15]X. Liu, *Liquid Jet Impingement on a Moving Wall*, Ph.D. thesis, The University of British Columbia (2022).
[16]F. C. Kohring, "Waterwall water-cooling systems," Iron and Steel Engineer **62**, 30–36 (1985).
[17]D. Zumbrunnen, "Convective heat and mass transfer in the stagnation region of a laminar planar jet impinging on a moving surface," (1991).
[18]D. Zumbrunnen, F. Incropera, and R. Viskanta, "A laminar boundary layer model of heat transfer due to a nonuniform planar jet impinging on a moving plate," Wärme-und Stoffübertragung **27**, 311–319 (1992).
[19]H. Glover, T. Brass, R. Bhagat, J. Davidson, L. Pratt, and D. Wilson, "Cleaning of complex soil layers on vertical walls by fixed and moving impinging liquid jets," Journal of Food Engineering **178**, 95–109 (2016).
[20]R. Bhagat, A. Perera, and D. Wilson, "Cleaning vessel walls by moving water jets: Simple models and supporting experiments," Food and Bioproducts Processing **102**, 31–54 (2017).
[21]D. T. Eadie, D. Elvidge, K. Oldknow, R. Stock, P. Pointner, J. Kalousek, and P. Klauser, "The effects of top of rail friction modifier on wear and rolling contact fatigue: Full-scale rail–wheel test rig evaluation, analysis and modelling," Wear **265**, 1222–1230 (2008).
[22]D. Eadie, J. Cotter, S. Iwnicki, K. Oldknow, and J. VanderMarel, "Locomotive fuel savings with top of rail friction control: connecting theory and field results," Ind. Railw **1**, 335 (2013).
[23]S. Chiu-Webster and J. Lister, "The fall of a viscous thread onto a moving surface: a 'fluid-mechanical sewing machine'," Journal of Fluid Mechanics **569**, 89–111 (2006).
[24]A. Hlod, A. Aarts, M. PELETIER, *et al.*, "Mathematical model of falling of a viscous jet onto a moving surface," European Journal of Applied Mathematics **18**, 659–677 (2007).
[25]M. Gradeck, A. Kouachi, A. Dani, D. Arnoult, and J.-L. Borean, "Experimental and numerical study of the hydraulic jump of an impinging jet on a moving surface," Experimental thermal and fluid science **30**, 193–201 (2006).
[26]B. Keshavarz, S. I. Green, M. H. Davy, and D. T. Eadie, "Newtonian liquid jet impaction on a high-speed moving surface," International Journal of Heat and Fluid Flow **32**, 1216–1225 (2011).
[27]B. Keshavarz, S. I. Green, and D. T. Eadie, "Elastic liquid jet impaction on a high-speed moving surface," AIChE journal **58**, 3568–3577 (2012).
[28]J. Moulson and S. Green, "Effect of ambient air on liquid jet impingement on a moving substrate," Physics of Fluids **25**, 102106 (2013).
[29]Y. Guo, *Newtonian and Viscoelastic Liquid Jet Impingement on a Moving Surface*, Master's thesis, The University of British Columbia (2014).
[30]Y. Guo and S. Green, "Visualization of high speed liquid jet impaction on a moving surface," Journal of Visualized Experiments , e52603 (2015).
[31]G. P. Association *et al.*, *Physical properties of glycerine and its solutions* (Glycerine Producers' Association, 1963).
[32]ANSYS, Inc., *ANSYS Fluent User's Guide*.
[33]J. U. Brackbill, D. B. Kothe, and C. Zemach, "A continuum method for modeling surface tension," Journal of computational physics **100**, 335–354 (1992).
[34]P. J. Roache, "Perspective: a method for uniform reporting of grid refinement studies," (1994).
[35]L. F. Richardson and J. A. Gaunt, "Viii. the deferred approach to the limit," Philosophical Transactions of the Royal Society of London. Series A, containing papers of a mathematical or physical character **226**, 299–361 (1927).
[36]C. Josserand and S. T. Thoroddsen, "Drop impact on a solid surface," Annual review of fluid mechanics **48**, 365–391 (2016).
[37]J. Hao and S. I. Green, "Splash threshold of a droplet impacting a moving substrate," Physics of Fluids **29**, 012103 (2017).
[38]D. Wilson, H. Köhler, L. Cai, J.-P. Majschak, and J. Davidson, "Cleaning of a model food soil from horizontal plates by a moving vertical water jet," Chemical Engineering Science **123**, 450–459 (2015).
[39]A. Craik, R. Latham, M. Fawkes, and P. Gribbon, "The circular hydraulic jump," Journal of Fluid Mechanics **112**, 347–362 (1981).
[40]X. Lu, J. Cotter, and D. T. Eadie, "Laboratory study of the tribological properties of friction modifier thin films for friction control at the wheel/rail interface," Wear **259**, 1262–1269 (2005).
[41]G. E. G. Sterling, "An experimental study on jet impingement on a very high speed moving surface," (2012).